

## Coherent Small-Angle Scattering on a Bending-Magnet Beamline at the ESRF

F. Livet,<sup>a\*</sup> F. Bley,<sup>a</sup> A. Létoublon,<sup>a</sup> J. P. Simon<sup>a</sup> and J. F. Béjar<sup>b</sup>

<sup>a</sup>LTPCM-ENSEEG, UMR-CNRS/INPG/UJF No. 5614, BP 75, 38402 St Martin d'Heres, France, and <sup>b</sup>Laboratoire de Cristallographie, CNRS, BP 166, 38402 Grenoble CEDEX, France

(Received 9 February 1998; accepted 22 May 1998)

A coherent X-ray beam is obtained from the D2AM bending-magnet beamline (BM2) of the European Synchrotron Radiation Facility. As this line has permanent convergent optics, monochromated by an Si(111) double monochromator, coherence conditions are satisfied by selecting a part of the beam close to the focal point. Low intensity ( $10^6$  X-rays  $s^{-1}$ ) is partially compensated by a high degree of coherence and by the use of a high-resolution direct-illumination CCD area detector. The stability of the small-angle set-up makes quantitative analysis possible. The calculated and measured degrees of coherence are compared. The distributions of speckle intensities are explained by a beam composed of two-thirds coherent and one-third incoherent parts. This incoherent component is caused by Kapton windows, which will be removed in future experiments.

**Keywords:** coherent X-rays; small-angle scattering; speckle.

### 1. Introduction

High-brilliance synchrotron radiation sources provide an excellent tool for obtaining coherent X-ray beams (Sutton *et al.*, 1991). This makes it possible to carry out experiments where short-wavelength X-ray beams are used like laser beams, mainly for speckle and X-ray photon correlation spectroscopy measurements in the Bragg peak region (Brauer *et al.*, 1995; Dufresne, 1995; Bley *et al.*, 1995) and in the small-angle domain (Dierker *et al.*, 1995; Mochrie *et al.*, 1997; Mainville *et al.*, 1997).

The basis of the improvements of third-generation synchrotron radiation machines is the high quality of electron optics at a few GeV. For instance, the initial ESRF goals were to obtain emittances of 7 nm (H)  $\times$  0.7 nm (V) for an intensity of 100 mA. Now (in 1997), one routinely obtains 4 nm (H)  $\times$  0.04 nm (V), with a 200 mA (nominal) intensity. This is an increase of a factor of 35 in brilliance, and this can induce a corresponding increase in available coherent beam intensities for undulator sources. In the case of bending-magnet sources, the beam divergence ( $\sim 10^{-4}$ ) is limited by the energy of the electrons (6 GeV), and only a decrease of the source size (from  $0.187 \times 0.128$  mm to  $0.142 \times 0.037$  mm) improves the brilliance. The total brilliance increase for a bending-magnet beamline is close to 12. At the same time, the beam stability has been improved in order that variations do not exceed 10% of the beam size and divergence. With such source performances, a demand exists for better X-ray optics and detectors.

For a monochromatic beam of wavelength  $\lambda$ , the basic technique for obtaining coherence is to fulfil the condition

$$\varepsilon\varphi \leq \lambda, \quad (1)$$

where  $\varepsilon$  is the beam divergence and  $\varphi$  is the beam size. In synchrotron radiation, the source size is fixed, and the simplest method can be to limit  $\varepsilon$  using slits. The synchrotron radiation source is smaller in the vertical direction ( $\varphi_v \simeq 40$   $\mu\text{m}$ ), and the corresponding transverse coherence length,  $\Lambda_t$ , for  $\lambda \simeq 1.5$   $\text{\AA}$ , at  $L \simeq 40$  m, is  $L\lambda/\varphi_v \simeq 150$   $\mu\text{m}$ . This coherence length is about four times smaller in the horizontal direction. If the whole coherent surface is selected, detection of the speckle structure needs an experimental resolution of the order of  $\lambda/\Lambda_t$ , here within the microradian range. In the available experiment set-up, the resolution is ten times larger. In this case, the size of the coherent beam must be less than 10  $\mu\text{m}$ . If no focusing optics are used, only a small part of the coherent available intensity is used, and the high quality of the source is useless. For this reason, focusing optics are an efficient improvement, provided that source degradation due to optical elements is not too strong.

In this paper we report tests with the D2AM beamline at the ESRF for coherent small-angle X-ray scattering (SAXS) experiments. This beamline is located on a bending-magnet source and has high-quality focusing optics. In this case, it is possible to control  $\varepsilon$  and  $\varphi$  simultaneously close to the focused image of the source. This makes possible a quantitative comparison between calculated and experimental intensities and coherence. The effect of inserting various devices into the beam is discussed (windows, monochromators, mirrors). This study

provides new ways for improving X-ray optics and X-ray detection, in order to take better advantage of the advances in the synchrotron radiation sources. Results are compared with the interpretation of experimental results (Abernathy *et al.*, 1998) from an undulator source beamline (Troika, ID10).

## 2. Characteristics of the beamline and the experimental set-up

### 2.1. Source

The brightness of the bending-magnet source can be estimated as (Elleau, 1986)

$$B \simeq 1.5 \times 10^{13} E^2 I \quad (2)$$

in photons  $s^{-1} \text{ mrad}^{-2}$  (0.1% bandwidth) $^{-1}$ . This formula holds roughly for  $0.8 < \lambda/\lambda_c < 3.0$ , where  $\lambda_c$  is the wavelength cut-off:  $\lambda_c = 0.64 \text{ \AA}$  for  $E = 6 \text{ GeV}$  and for a bending-magnet field of 0.85 T.  $I$  is the electron beam intensity ( $I = 0.02 \text{ A}$ ). In our experiment,  $\lambda = 1.56 \text{ \AA}$ , and we find

$$B = 1.1 \times 10^{14} \text{ photons } s^{-1} \text{ mrad}^{-2} (0.1\% \text{ bandwidth})^{-1}. \quad (3)$$

The brilliance,  $b$ , of the source can be deduced from the source dimensions given by ESRF data sheets (Roth *et al.*, 1997). In the case of  $\sigma_h = 142 \text{ }\mu\text{m}$  and  $\sigma_v = 37 \text{ }\mu\text{m}$  (r.m.s.), we find

$$b = B/(2\pi\sigma_h\sigma_v) = 3.3 \times 10^{15} \text{ photons } s^{-1} \text{ mrad}^{-2} \text{ mm}^{-2} (0.1\% \text{ bandwidth})^{-1}. \quad (4)$$

From this result, one can roughly estimate the maximum coherent intensity with an Si(111) double monochromator ( $\delta\lambda/\lambda = 1.4 \times 10^{-4}$ ), assuming  $\varepsilon\varphi = \lambda$ , as

$$I_0 = 0.14(1.56 \times 10^{-4})^2 b = 1.1 \times 10^7 \text{ photons } s^{-1}. \quad (5)$$

### 2.2. Optics

The D2 beamline has pseudo-symmetrical double-mirror–double-monochromator optics (Roth *et al.*, 1997). The incoming vertically diverging beam is made parallel by the first curved mirror in order to obtain an excellent monochromatization by the Si crystals. The second monochromator crystal is sagittally curved in order to focus the

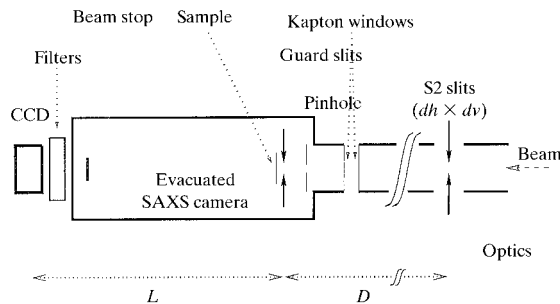


**Figure 1**  
Sketch of the SAXS set-up.

beam horizontally. As the dimensions of the beam can be 4 mm (V)  $\times$  80 mm (H), the second crystal is reinforced with ribs (period 1.2 mm) in order to limit antiscatter curvature. This results in a non-constant and periodic curvature. This is observed for underfocused configurations of the bent monochromator, where the image of the beam close to the sample consists of a horizontal alignment of spots, corresponding to the 1.2 mm period. One of these spots is selected by closing the primary slits S1 (23 m from the source) to  $1 \times 1 \text{ mm}$  in order to optimize the horizontal focusing. The heat load becomes negligible and this improves the experimental stability. The second mirror is a vertically focusing mirror and, as only a small region of the optics is used in this experiment, optical defects are less probable.

The quality of the focusing optics was tested for small beams. In this case, the final limitation of the beam is obtained by the S2 secondary slits, with an opening  $d_h \times d_v$ . The source-to-optics distance was 27 m and the  $10 \text{ }\mu\text{m}$  pinhole was used for scans after optimization of focusing. The pinhole was close to the sample position, 11 m after the centre of the optics and 9.5 m after S2. The image dimensions  $s_h$  and  $s_v$  (FWHM) were measured in two different configurations: (i) 1/3 filling, 124 mA,  $d_v \times d_h = 0.75 \times 1.0 \text{ mm}$ ,  $s_h = 112 \text{ }\mu\text{m}$ ,  $s_v = 59 \text{ }\mu\text{m}$ ; (ii) 16 bunches, 90 mA,  $d_v \times d_h = 0.2 \times 0.2 \text{ mm}$ ,  $s_h = 90 \text{ }\mu\text{m}$ ,  $s_v = 55 \text{ }\mu\text{m}$ .

Focusing is better in the second configuration. This is mainly the result of closing the secondary slits S2, which minimize optical defects. The (FWHM) area of the beam can be *a-priori* estimated from the (r.m.s.) dimensions of the source and from the ratio between the source-to-optics distance and the optics-to-pinhole distance (2.5 here). This area is  $\sigma_h \times \sigma_v \times (8 \ln 2)/(2.5)^2 = 4.7 \times 10^{-3} \text{ mm}^2$ , which compares well with the best value given here, namely  $s_h \times s_v = 5 \times 10^{-3} \text{ mm}^2$ . The focusing optics can be considered as excellent.

### 2.3. Coherence

In this type of experiment, the number of optical elements is usually minimized in order to limit distortions of the beam. Each of these optical elements acts as a secondary source, so that stable and reliable speckle structures are difficult to obtain. In our case, as permanent focusing optics are present, we take advantage of the large distance ( $\sim 10 \text{ m}$ ) between slits S2 at the end of the optics and the SAXS camera. Coherence conditions will be discussed by considering the square ( $d_h = d_v = d$ ) beam across slits S2 as a secondary source. The experimental set-up is sketched in Fig. 1. The pinhole limiting the beam size, of diameter  $\varphi$ , is placed at the entrance of the SAXS camera, at a distance  $D = 9.5 \text{ m}$  from S2. Transverse coherence will be obtained by choosing suitable values of the ratio

$$z = \pi d\varphi/2\lambda D. \quad (6)$$

This ratio will be essential for the quantitative discussion.

Due to excellent monochromaticity, the longitudinal coherence length,  $\Lambda_l = \lambda/(\delta\lambda/\lambda)$ , is of the order of 1  $\mu\text{m}$ . For small-angle experiments (here  $2\theta$  is less than 0.01 rad), with pinhole diameters  $\varphi \leq 10 \mu\text{m}$ , and sample thicknesses  $e \leq 1 \text{ mm}$ , it can be assumed that the conditions of coherence are met (roughly  $\varphi\theta \ll \Lambda_l$  and  $e\theta^2 \ll \Lambda_l$ ).

#### 2.4. Windows

Transmission through windows has strong effects on the beam coherence. There are two 500  $\mu\text{m}$ -thick Be windows on the beam; the first is before the optics and the second is between the first mirror and the monochromators. There is a 50  $\mu\text{m}$ -thick Kapton window just before slits S2. For vacuum security, two thin Kapton windows (thicknesses 20  $\mu\text{m}$  and 50  $\mu\text{m}$ ), separated by 1.5 cm of air, are placed 41 cm before the pinhole.

#### 2.5. SAXS camera

The SAXS camera is housed in an evacuated cell. The pinhole holder is followed, after 21 cm, by guard slits (S4). Samples can be placed just after these slits. The beam stop is at a distance of 2.1 m from the sample, just before the end of the evacuated tube. A filter holder is inserted before the detector.

#### 2.6. Detection

A 'deep depletion' CCD area detector from Princeton Instruments was used in direct X-ray illumination. The pixels are squares of size  $r_0 = 22.5 \mu\text{m}$ . At 2.2 m from the sample, the pixel resolution of the CCD (10  $\mu\text{rad}$ ) is sufficient to resolve the speckle structure ( $\lambda/\varphi = 15.6 \mu\text{rad}$  for  $\varphi = 10 \mu\text{m}$ ). For a  $576 \times 384$  pixel area, the detector surface is of the order of  $1 \text{ cm}^2$ . The absorption of an X-ray on the surface of the CCD creates very locally about 2000 electronic charges which, as the detector is cooled at 213 K, is more than 100 times larger than the noise. It is easy to calculate the position (Livet *et al.*, 1998) of isolated X-rays with an accuracy of 1 pixel. A custom-designed 'droplet' program has been developed that extracts the position of individual photons from images obtained by frequent readings of the detector. With this program, the analog CCD device is transformed into an area photon-counting detector. The overall detection quantum efficiency (DQE) of the detector is estimated to be 55% at the 7.95 keV photon energy used here.

### 3. Results

#### 3.1. Diffraction of the pinholes

One of the standard methods for checking coherence properties of the experiment is to observe Fraunhofer fringes from the pinholes used for the selection of the coherent beam.

In these tests, electron microscopy pinholes were used. The advantage of these is the high quality of their edges, as can be verified by scanning electron microscopy. For their use in X-ray beam selection, these pinholes have relatively

thin edges (here, close to 10  $\mu\text{m}$ ). The hole is at the centre of a conical hollow in a  $\text{Pt}_{0.95}\text{Ir}_{0.05}$  80  $\mu\text{m}$ -thick sheet. Simple calculations show that at 7.95 keV the fraction of X-rays crossing the edges of the aperture is less than 3% for the 10  $\mu\text{m}$  pinhole diameter, and we neglect this effect. This contribution will, however, increase rapidly with photon energy.

The pinhole-detector distance is  $L = 2.41 \text{ m}$ , and the measured intensity is strongly localized at the centre of the detector. For that reason, an attenuation by a factor of  $10^3$  to  $10^4$  is necessary, and the recorded region of the detector is limited to an area of  $100 \times 100$  pixels. This reduces the total time for ADC conversion and for disk-saving to about 0.1 s with a 430 kHz ADC unit and a standard Pentium-based PC computer.

In practice, 2000 frames of 0.03 s each were recorded, each one corresponding to a few hundred detected X-rays. Our 'droplet' program was then used. For each frame, the position of each X-ray was registered. Frames were then deleted and a new measurement started.

For studies where time resolution is not required, the number of detected X-rays for each pixel is eventually accumulated. The centre of the pattern ( $x_0, y_0$ ) is calculated from the first moment of the distribution. The distance  $R$  of each pixel to the centre of the pattern can be deduced.

A series of results obtained with the 10  $\mu\text{m}$  pinhole are plotted in Fig. 2 with various values of  $d$ , the aperture of the secondary slits S2: for (a), (b), (c), (d) and (e),  $d = 50, 100, 150, 200$  and  $300 \mu\text{m}$ , respectively. Averages have been taken along right and left half-circles, and  $R$  was incremented by 0.25 of a pixel. In Figs. 2(a) and 2(b), Fraunhofer fringes are clearly visible, and there is no significant difference between the two images. Only the different number of accumulated X-rays [ $3.4 \times 10^5$  and  $7.5 \times 10^5$  for Figs. 2(a) and 2(b), respectively] accounts for the greater noise in the case of Fig. 2(a). The dynamics of the observed intensities is close to five orders of magnitude. Plots of  $IR^3$  [Figs. 2(f)–2(j) corresponding to Figs. 2(a) to 2(e)] allow a detailed discussion of the results. The asymptotic behaviour of our measurements can be compared with the asymptotic shape of the diffraction pattern of a pinhole of diameter  $\varphi$  at a distance  $L$  from the detector plane,

$$IR^3 \propto 1 - \sin(2\pi R\varphi/\lambda L). \quad (7)$$

In Fig. 2, the distances  $R$  are expressed in pixel units:  $n = R/r_0$ . From the period of the oscillations, a precise estimate of  $\varphi$  can be given:  $\varphi = 9.35$  (5)  $\mu\text{m}$ , which is close to the nominal 10  $\mu\text{m}$  diameter. Many oscillations can be observed in Figs. 2(f) and 2(g). This means that the diameter is well characterized and that the edges of the hole are of good quality. Moreover, the curves are very symmetrical, showing that, in the region of the CCD shown in Fig. 2 (60 pixels diameter, *i.e.* 1.3 mm on the CCD), scattering from the surface of the hole is negligible. Irregular intensity tails are observed for larger  $R$  values, and closing of the guard slits (S4) to 70  $\mu\text{m}$  suppresses this parasitic scattering.

Although the oscillations in Figs. 2(f) and 2(g) are not damped, their amplitudes are about 40% of the predicted value. One of the reasons for this is the lack of resolution due to the pixel size. The period of the oscillations is 1.79 pixels. If one approximately calculates the amplitude of the oscillations from the pixel resolution, one obtains

$$IR^3 \propto 1 - 0.56 \sin(2\pi R\varphi/\lambda L). \quad (8)$$

This partly explains the small amplitude of the oscillations. In Figs. 2(c), 2(d) and 2(e) the Fraunhofer oscillations become indistinguishable and the FWHM of the beam increases. A simple formula for that width is

$$s_R = L[(\lambda/\varphi)^2 + (d/D)^2]^{1/2}. \quad (9)$$

This equation is a first approximation for the beam coherence. Pinhole refraction effects are dominant when the

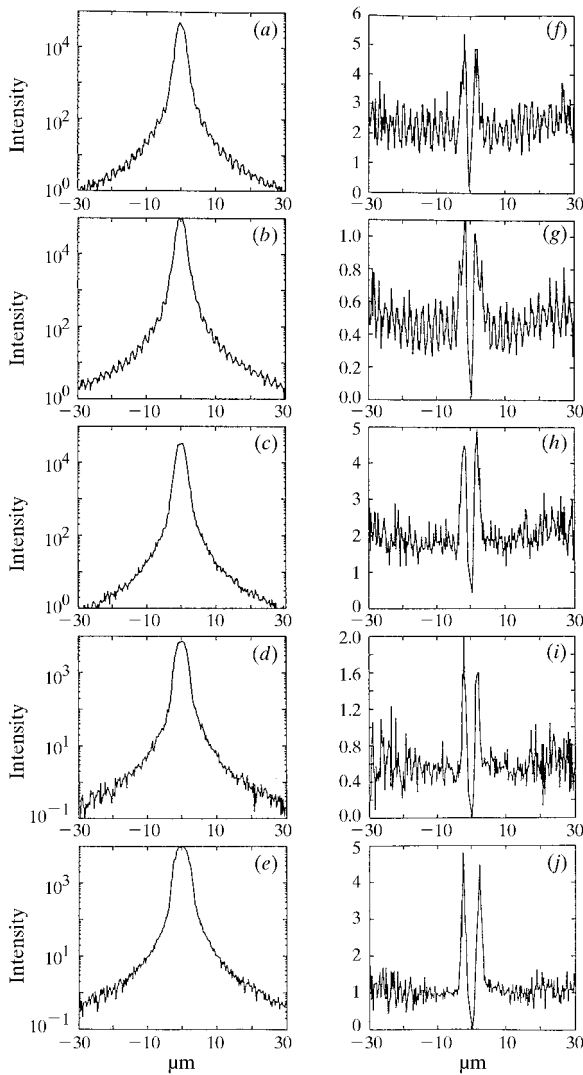


**Figure 2**

Images on the CCD area detector of the beam crossing the 10  $\mu\text{m}$  pinhole. Intensities have been averaged on semicircles around the origin, with 0.25 pixel steps. Results are left/right symmetrical, and the oscillations are stronger with better coherence conditions:  $z$  (see Table 1) varies from 0.5 to 3 from top to bottom. On the right-hand side,  $IR^3$  is plotted, showing asymptotic behaviour. See text.

**Table 1**

Characteristics of the beam across pinholes for various beam divergences.

Passage from diffraction-dominated width ( $z \leq 1$ ) to mixed mode ( $z > 1$ ).  $s_R$  is taken from equation (9)

$\varphi$ ( $\mu\text{m}$ )	$d$ ( $\mu\text{m}$ )	$z$	FWHM ( $\mu\text{m}$ )	$s_R$ ( $\mu\text{m}$ )
10	50	0.5	49	40
10	100	1.0	51	45
10	150	1.5	59	54
10	200	2.0	71	63
10	300	3.0	81	85
5	100	0.5	83	79
5	300	1.5	108	107

dimensionless ratio  $z$  in equation (6) is small:  $z = 0.5$  and 1.0 for Figs. 2(a) and 2(b), respectively.

A similar discussion may be applied to the 5  $\mu\text{m}$  pinhole. In Fig. 3(a),  $d = 100 \mu\text{m}$  and  $z = 0.5$ , and the oscillations are visible with a larger period as expected. In Fig. 3(b),  $d = 300 \mu\text{m}$ , and  $z = 1.5$ , and the oscillations are difficult to observe.

Table 1 shows the observed beam FWHM and the results of equation (9), as a function of  $\varphi$  (and  $z$ ). Agreement is satisfactory, if account is taken of the 22.5  $\mu\text{m}$  pixel resolution.

From filter transmission, the beam intensity for the 10  $\mu\text{m}$  pinhole and  $d = 200 \mu\text{m}$  is about  $10^6$  X-rays  $\text{s}^{-1}$ , for a 200 mA electron beam in the storage ring. As the product  $\varepsilon\varphi$  is here close to  $\lambda$  ( $1.5\lambda$ , in fact), this value is to be compared with that calculated from the source characteristics,  $1.1 \times 10^7$ .

The coherence of the beam is difficult to estimate quantitatively from these patterns. Better estimates are obtained from test samples.

### 3.2. Quantitative study of coherence

**3.2.1. Sample.** In order to discuss the beamline capacity for obtaining SAXS speckle patterns, scattering from a

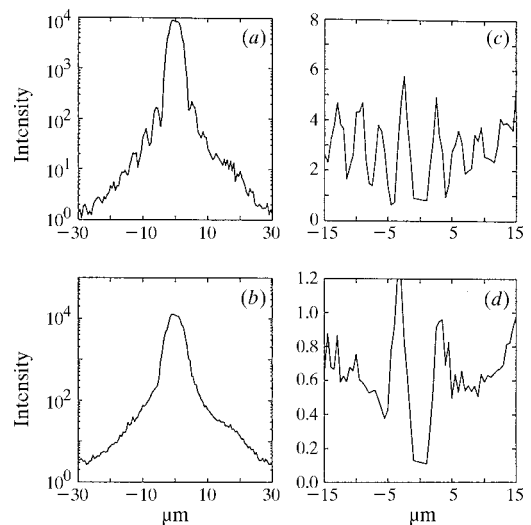


**Figure 3**

Same as Fig. 2 for the 5  $\mu\text{m}$  pinhole ( $z$  varies from 0.5 to 1.5).

0.5 mm-thick Teflon test sample was measured. The sample-to-CCD distance was  $L = 2.2$  m. The guard slits were closed to  $70 \mu\text{m}$  so that, with a 2 mm diameter beamstop located 10 cm before the CCD, the X-ray background was negligible.

The whole detector area was used, and the ‘droplet’ algorithm was applied to 1000 or 2000 frames of 1 s or 2 s each. For such times, the maximum intensity was of the order of  $10^{-2}$  X-rays  $\text{pixel}^{-1} \text{frame}^{-1}$ .

In a standard (incoherent) experiment, Teflon has an isotropic scattering pattern. This intensity,  $\langle I(q) \rangle$ , can be obtained from a circular average of the intensity across the area detector.

For example, in Fig. 4  $\langle I(q) \rangle$  is plotted for the  $q$ -region discussed here. The units are counts  $\text{pixel}^{-1}$ , and the results correspond to an accumulation of 1000 frames of 2 s each, with  $d = 100 \mu\text{m}$  and a  $10 \mu\text{m}$  pinhole. The electron beam intensity was 80 mA (16-bunch mode). The averages were carried out over circular bands 3 pixels wide. This provides a reasonable number of pixels (from 1000 to 2000), and the incoherent intensity varies negligibly across these regions. The average number of photons per pixel is low (from 2 to 20 for a total counting time of 30 min), and Poisson statistics have to be taken into account for a quantitative discussion.

**3.2.2. Coherence and statistics.** Among regions of constant  $\langle I \rangle$ , coherence leads to strong variations of measured intensity. For full coherence, the intensity probability distribution is

$$p(I) = \exp(-I/\langle I \rangle)/\langle I \rangle. \quad (10)$$

In the case of partial coherence, it can be assumed that the scattering observed corresponds to a set of  $\alpha$  ( $\alpha$  need not be an integer) identical ‘coherence volumes’ scattering inde-

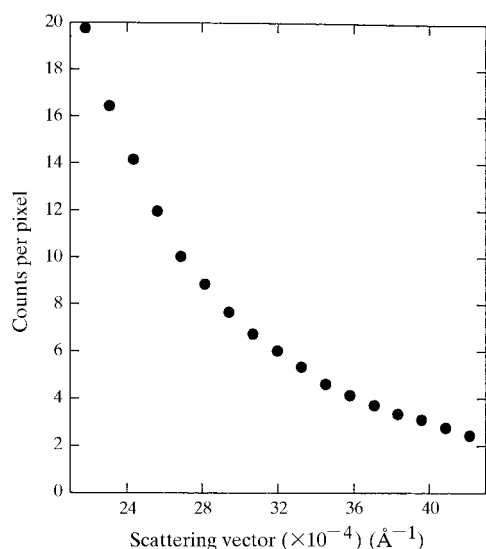


**Figure 4** Circularly averaged intensity from a Teflon sample. Here,  $z = 1$ , and  $d = 100 \mu\text{m}$ ,  $\varphi = 10 \mu\text{m}$ , 2000 s acquisition time for an 80 mA electron beam intensity.

pendently (ICV assumption). The usual methods of statistical convolution (Brown, 1993) lead to the distribution

$$p_\alpha(I) = I^{\alpha-1} \exp(-I/I_0)/[\Gamma(\alpha)I_0^\alpha], \quad (11)$$

where  $I_0 = \langle I \rangle/\alpha$  and the global degree of coherence of the experiment is  $\beta = 1/\alpha < 1$ .

**3.2.3. Calculated coherence from experimental geometry.** In order to test the ICV hypothesis,  $\beta$  has to be calculated. The result will be compared with experimental estimations. We have to consider two averaging processes leading to  $\beta < 1$ . First, we use Young’s technique, where a small angular region of an incoherent source (here the beam across S2) is selected. This always leads to partial coherence. Second, the speckle structure is somewhat averaged by the finite size of the CCD pixel. As  $\varphi < (r_0, d)$ , we will consider these two averages as statistically independent.

The beam coherence,  $\beta_b$ , can be obtained from the complex mutual coherence,  $\mu(r)$ , between two points at distance  $r$  in the pinhole plane.  $\mu(r)$  corresponds to the beam radiated by slits S2, acting as a secondary source. The average over the pinhole surface has to be calculated:  $\beta_b = \langle |\mu(r)^2| \rangle$ . The intensity across S2 must be assumed to be uniform, but the shape of the wavefront is not planar: the beam is convergent. On the other hand, as the beam is focused, it can be considered to be planar close to the pinhole. For this reason,  $\beta_b$  is calculated in the reverse manner: the pinhole is considered as a planar incoherent secondary source, and mutual coherence is obtained between two points in the plane of S2, separated by a distance  $x$  (Mandel & Wolf, 1995),

$$\mu(x) = 2J_1(\pi x \varphi / 2\lambda D) / (\pi x \varphi / 2\lambda D), \quad (12)$$

and  $\beta_b$  is estimated by averaging  $|\mu(x)^2|$  across slits S2,

$$\beta_b(z) = 1 - z^2/6 + 7z^4/432 - z^6/960 + \dots, \quad (13)$$

where  $z$  is defined in equation (6).

The intensity radiated by the sample is averaged by the detector. This contribution,  $\beta_d$ , can also be obtained by averaging  $|\mu(x)^2|$  over the pixel size. The values of  $\mu(x)$  are also calculated by considering the beam across the pinhole as a planar incoherent secondary source. The pinhole-sample distance can be neglected. From detector resolution ( $r_0 = 22.5 \mu\text{m}$ ),  $z = \pi \varphi r_0 / 2\lambda L \simeq 1$  and, from (13),  $\beta_d = 0.85$ .

The global degree of coherence of the experiment can be expressed as the product of the two averages, *i.e.*  $\beta_0 = \beta_b \beta_d$ . This assumes that no correlation occurs, on average, between the two calculated values of  $\mu(r)$ . The result of the calculation is given in Table 2 for the set of values of  $d$  where scattering from Teflon has been measured. As  $d$  varies from 100 to 250  $\mu\text{m}$ , and as only the  $10 \mu\text{m}$  pinhole was used,  $z$  lies between 1 and 2.5.

In the case of low  $z$ , the result of the calculation depends only weakly on the exact shape of the beam. It is not necessary to know precisely the intensity and phase across the incoherent source S2. For instance,  $\beta_b$  was also estimated for a planar source across slit S2,

**Table 2**

Various estimates of coherence.

$\varphi = 10 \mu\text{m}$ .  $\beta_0 = \beta_b \beta_d$  from geometry of experiment,  $\beta_a$  from MSD, and  $\delta$  and  $\beta$  from hybrid model.

$d$ ( $\mu\text{m}$ )	$z$	$\beta_0 = \beta_b \beta_d$	$\beta_a$	$\delta$	$\beta$	$z^2 \beta_b$
100	1.0	0.719	0.31	0.37	0.72	0.85
150	1.5	0.590	0.28	0.37	0.60	1.56
200	2.0	0.456	0.19	0.37	0.47	2.15
250	2.5	0.348	0.15	0.37	0.35	2.56

$$\beta_b(z) = 1 - z^2/6 + 17z^4/1080 - 29z^6/30240 + \dots \quad (14)$$

This expansion is very similar to (13).

### 3.2.4. Simple estimation of coherence from the experiment.

The coherence can be estimated from the mean square deviation (MSD) of the intensity around circles,

$$\langle I^2(q) \rangle - \langle I(q) \rangle^2 = \beta_a \langle I(q) \rangle^2 + \langle I(q) \rangle. \quad (15)$$

As the Poisson counting statistics are independent of electromagnetic field fluctuations, its corresponding contribution is added to the MSD estimate. In this equation,  $\beta_a$  is an apparent coherence.

$\beta_a$  is usually obtained from a plot of  $\{\langle I^2(q) \rangle - [\langle I(q) \rangle]^2\} / \langle I(q) \rangle$  versus  $\langle I(q) \rangle$ . The constant slope of the plot gives an estimate of  $\beta_a$ , the error of which is close to 0.01 here, and which provides a test of the experimental stability. Such a plot is shown in Fig. 5 for the same results as in Fig. 4. Here,  $\beta_a = 0.31$  (1) and the calculated value of  $\beta$  is 0.72. Such a discrepancy is observed for all the results: all  $\beta_a$  are about 2.5 times lower than  $\beta_0$ . Obviously,  $\beta_a$  is large enough to observe speckle patterns. This nevertheless leads to a strong decrease in the signal-to-noise ratio and, for the same intensity, it takes 2.5 times longer for the same speckle contrast measurement. Moreover, if the shape of the incoming electromagnetic waves is not fully understood, improvements in the beam and sample stability can

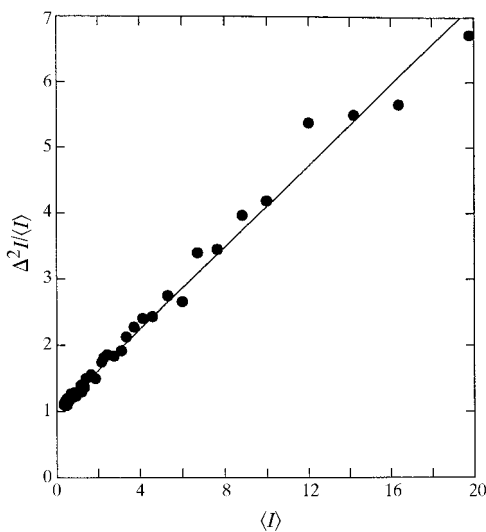


**Figure 5**  
Plot of  $\Delta^2 I / I$  versus  $I$ . The slope (0.31) gives an estimate of the apparent degree of coherence  $\beta_a$ .

be difficult, as well as the interpretation of static measurements.

### 3.2.5. A detailed statistical study of intensity distribution.

One of the origins of the low value of  $\beta_a$  can be mechanical instabilities. In fact, after a few hours a non-linear shape is observed on the curves as in Fig. 6. For low intensities, corresponding to large angles ( $q \simeq 8 \times 10^{-3} \text{ \AA}^{-1}$ ), after some hours the slope of the plot decreases indicating long-term drift of the experiment. This is the only evidence of instability observed, and an intensity decrease is simultaneously observed. This intensity decrease can be compensated by a  $\pm 30 \mu\text{m}$  vertical movement of the second mirror, indicating that instabilities are related mainly to fluctuations in the optics alignment. An approximative daily cycle was observed. The SAXS experiment (including pinholes and detector) is itself mounted on a monolithic granite optical bench and is very stable. This type of support can, however, experience vibrations with a period shorter than the time resolution of 1 s. The main effect of vibrations is to increase the number of coherence volumes (McKechnie, 1975). As in this case, equation (11) should hold with  $\alpha = 1/\beta_a$ ; this hypothesis can be tested by studying the intensity distribution.

In order to compare equation (11) with the observed intensity probability distribution, it is necessary to take account of Poisson counting statistics, and the probability of obtaining a discrete value of  $k$  for  $I$  is calculated by a Poisson transform (Mandel formula),

$$p_a(k) = \Gamma(k + \alpha)(1 + 1/I_0)^{-(k+\alpha)} / [\Gamma(k + 1)\Gamma(\alpha)I_0^\alpha]. \quad (16)$$

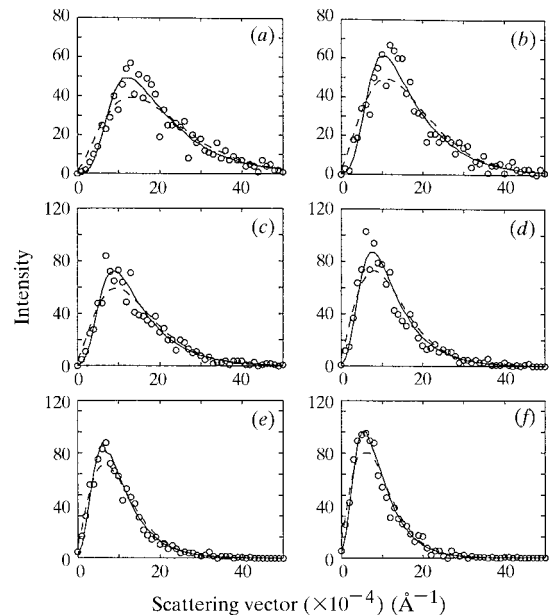


**Figure 6**  
Intensity distributions (circles) observed for the six larger average intensities ( $q$  varies from  $2.1 \times 10^{-3} \text{ \AA}^{-1}$  to  $2.8 \times 10^{-3} \text{ \AA}^{-1}$ ) of Fig. 4. Dashed lines show the standard model of partial coherence and continuous lines show the hybrid model described in the text.

Fig. 6 compares the observed and calculated distributions for various angles for the same results as Fig. 4. The six curves correspond to the six upper points of the figure. The dotted curves are obtained from (16), with  $\alpha = 1/\beta = 3.2$ , as discussed earlier with reference to Fig. 5. As has been already observed (Abernathy *et al.*, 1998), the calculated distribution does not fit the results: the number of low counts is too small, and the observed distribution is more peaked than that calculated. Only the tail of the curve fits well.

The shape of the distribution can be better discussed in terms of moments. Fig. 7 compares the calculated second-order moment of the distribution [equation (15)] (same results as Fig. 4) with the right-hand side of equation (15) (dotted line, with  $\beta_a$  from Table 2). Obviously, the fit with  $\beta_a = 0.31$  is excellent. From the third and fourth moments, the skewness is calculated (Mandel & Wolf, 1995) from the integer values of  $I(q)$ ,

$$\frac{\langle [I(q) - \langle I(q) \rangle]^3 \rangle / \langle [I(q) - \langle I(q) \rangle]^2 \rangle^{3/2}}{2/\alpha^{1/2} + O[1/\langle I(q) \rangle^2] + \dots}, \quad (17)$$

and from the kurtosis, from which we subtract the Gaussian constant 3,

$$\frac{\langle [I(q) - \langle I(q) \rangle]^4 \rangle / \langle [I(q) - \langle I(q) \rangle]^2 \rangle^2 - 3}{6/\alpha + O[1/\langle I(q) \rangle^2] + \dots}, \quad (18)$$

where Poisson counting statistics introduce correcting second-order terms  $\{O[1/\langle I(q) \rangle^2]\}$ , which are calculated numerically. Results of these two calculations are given in Figs. 8 and 9. Open circles correspond to the results of Fig. 4 and closed circles correspond to a second measurement under identical conditions. The comparison between the results of the two measurements (dotted line) and the results of equations (17) and (18), with  $\alpha = 1/\beta_a$  (Table 2), clearly shows a discrepancy. In both cases, the experimental

results are larger than calculated. Moreover, extrapolation towards low angles (large intensities) should provide an estimate of  $2/\alpha^{1/2} \simeq 1.6$  [equation (17)] and  $6/\alpha \simeq 3.8$  [equation (18)]. This is consistent with  $\beta = 0.64$ , much larger than  $\beta_a = 0.31$ , and closer to  $\beta_0 = 0.72$  of Table 2. Skewness and kurtosis are independent of the average value of a distribution. This means that a constant shift of the origin of  $I$  gives a distribution that is in better agreement with the predicted distribution.

**3.2.6. Two beam components.** A more realistic statistical model can be deduced from this discussion. Following Abernathy *et al.* (1998), we assume that the incoming beam can be decomposed into two different contributions. The first, of relative intensity  $\delta$ , is completely incoherent and gives incoherent small-angle scattering with only Poisson statistics. The second contribution, of relative intensity  $1 - \delta$ , is partially coherent with a degree of coherence  $\beta$ . Qualitatively, this model explains why low counts are rarely observed (see Fig. 6). The corresponding distribution has been calculated taking account of Poisson counting statistics contributions. Typical results are shown in Fig. 6 (continuous lines) for the distributions and in Figs. 8 and 9 for the moments, with  $\delta = 0.37$  and  $\beta = 0.72$ . The hybrid model explains the observed distribution. In Fig. 7, the continuous line corresponds to the two-beam model, and it is observed that the second-order moment cannot distinguish between the two models discussed here: they both fit the experimental results.

This model was applied to all the measurements of Table 2. All the results agree well with a constant incoherent component,  $\delta \simeq 0.37$ , of the beam. In this case,  $\beta$  is in agreement with our estimates ( $\beta_0$ ) from the geometry of the experiment. Although standard coherence theory cannot

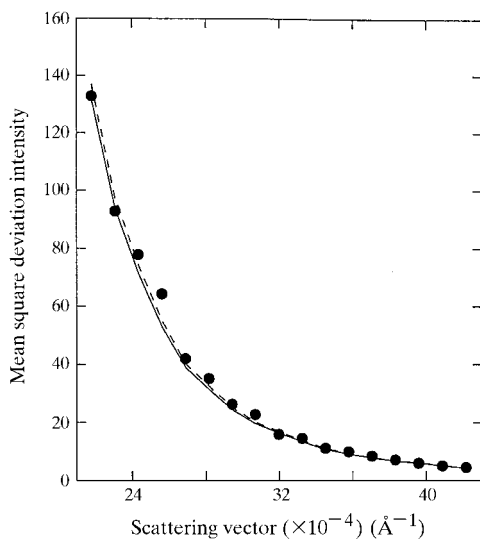


**Figure 7** Observed (circles) and calculated angular mean square deviations. Same results as Fig. 4 and same symbols as Fig. 6.

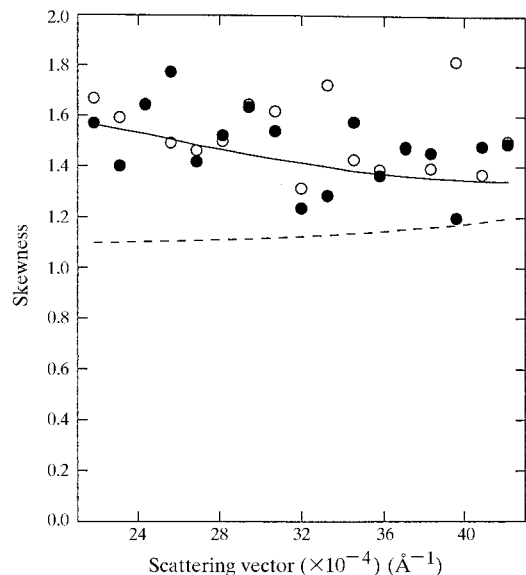


**Figure 8** Experimental (open and filled circles) and calculated skewness. Same conditions as Fig. 4. Two results are shown in order to estimate standard deviations. The hybrid model (continuous line) is more consistent with the data than the classical model (dashed curve).

explain the presence of the incoherent beam, this latter has an intensity that is proportional to the incoming beam. It seems obvious that there is a secondary source that re-emits X-rays under irradiation. This explains the reduction of  $\beta$ :  $\beta_a \simeq \beta_0(1 - \delta)^2 \simeq \beta_0/2.5$ .

**3.2.7. Windows.** The only possible secondary source is the two thin Kapton windows (20 and 50  $\mu\text{m}$ ). These are close to the focus, and one can consider that the irradiated area is 100  $\mu\text{m}$  (H)  $\times$  50  $\mu\text{m}$  (V) (FWHM). These windows are about 41 cm before the pinhole. Normally, such windows have only a low absorption, and Kapton is not usually considered as a strong scatterer. In fact, the SAXS intensity is relative to the  $q$ -region considered. In the case of these windows, if they scatter strongly in a cone of angle  $10^{-4}$  rad (in  $2\theta$  units), they give a strong contribution to the intensity crossing the pinhole. This intensity has very poor coherence (the corresponding value of  $z$  is close to 10). Conversely, a significant part of the beam travelling towards the pinhole is slightly deviated and lost from the experiment. Obviously, this picture is simplified: the whole beam wavefront is distorted on passing through the windows.

This incoherent component of the beam crossing the pinhole can also contribute to the low amplitude of the intensity oscillations in Figs. 2(f) and 2(g).

### 3.3. Intensity/coherence optimization

If no incoherent scattering is observed, a high value of  $\beta$  can be obtained by closing slits S2. This is obviously at the expense of intensity, and practical criteria for the experiment can be briefly discussed.

The experimental speckle contrast is of the order of  $\langle I(q) \rangle \beta(z)^{1/2}$ . Because it depends on the number of coherence areas,  $\beta(z)$  decreases as  $z^{-2}$  for large  $z$ , and  $\langle I(q) \rangle$

increases as  $z^2$ . We are interested in the square of the signal-to-noise ratio (s/n), where

$$(s/n)^2 = [\beta \langle I(q) \rangle^2] / \langle I(q) \rangle \simeq z^2 \beta_b(z), \quad (19)$$

where the square of the Poisson counting noise is  $\langle I(q) \rangle$ . Starting from the calculated coherence [equation (13) gives the first terms of the series expansion], the product  $z^2 \beta_b(z)$  is  $\pi$  for  $z = \infty$ . Results for the  $z$  values of interest are given in Table 2. The values of the product still show a significant increase for  $z > 2$ . For instance, the condition  $z = 2$  means  $\beta_b = 0.53$ , and the product is 2.15, which is significantly smaller than  $\pi$ . For  $z = 3$ ,  $\beta_b = 0.28$ , and the product is 2.6. For these values, pinhole Fraunhofer oscillations are difficult to observe (see Fig. 2). This means that the observation of these oscillations is not necessary for the experimental study of speckle contrast. In practice,  $z$  cannot be very large. In our case,  $z$  is varied by opening slits S2, and inhomogeneities or instabilities of the beam may also have a strong influence. As a 25% speckle contrast is often considered to be excellent,  $z$  may range from 2 to 3 in practical experiments, if incoherent scattering is eliminated.

### 3.4. Beam intensity

The quality of the source is in agreement with the ESRF data sheets, and no significant degradation is observed after the focusing optics. This latter was originally designed to obtain a stable focus size of 300  $\mu\text{m} \times 300 \mu\text{m}$  (1/10  $\text{mm}^2$ ) and, provided that only a small fraction is used, we obtain a stable FWHM area of 1/200  $\text{mm}^2$ .

The beam intensity was observed to be about  $10^6$  photons  $\text{s}^{-1}$  for  $\varepsilon\varphi \simeq 1.3\lambda$  ( $z \simeq 2$ ). The intensity estimated from the source characteristics is  $1.1 \times 10^7$  photons  $\text{s}^{-1}$ . Some losses have been neglected: for beryllium windows ( $\sim 0.1$  mm), for which we calculate a transmission of 0.75, the reflectivity of each mirror is roughly 70%, yielding a total loss factor of 3. This leaves a residual factor of about 4. As the focus is excellent, the mirror and the monochromator optical elements are clear of suspicion.

The main explanation for this intensity loss can be found in the above discussion. There are two unpolished beryllium windows prior to the monochromator and a Kapton window after the optics, before slits S2. The intensity diffracted at very small angles by these windows is completely eliminated in the case of the very high experimental resolution needed here. Qualitatively, this means that a large fraction of the improvements in synchrotron radiation source performance are lost because of these windows.

## 4. Discussion

We can now briefly compare these results with those obtained on an ESRF undulator beamline (Troika), as discussed by Mainville *et al.* (1997) and Abernathy *et al.* (1998). In the latter paper, the degree of coherence is estimated for a very different set-up: (i) by means of plane mirrors, a wide energy bandwidth ( $\delta\lambda/\lambda = 1.3\%$ ), corre-

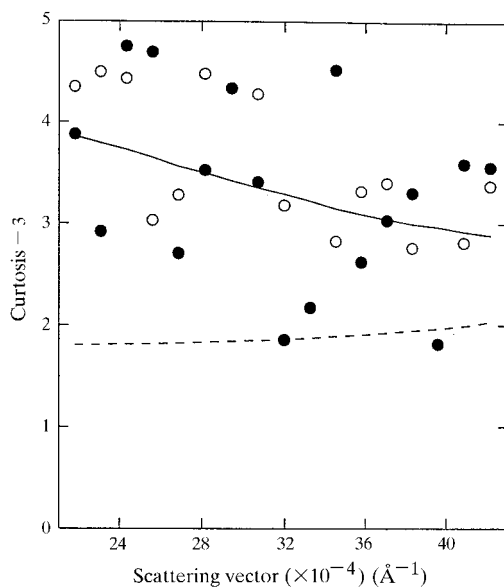


**Figure 9** Curtosis (with the Gaussian constant 3 subtracted). Same symbols and results as Fig. 8.

sponding to the third harmonic of the undulator, is selected, and the beam intensity is three orders of magnitude larger ( $10^9$  photons  $\text{s}^{-1}$ ); (ii) the main causes of loss of coherence are the windows which decrease  $\beta$  by a factor of 10 (Abernathy *et al.*, 1998), and the energy bandwidth which decreases  $\beta$  by a factor of 3 for  $q \simeq 0.01 \text{ \AA}^{-1}$ . This also explains the elongated shape of the speckles observed.

The brilliance of an undulator is  $10^3$  times greater than that of a bending-magnet beamline, and this is sufficient to explain the observed intensity difference.

Apart from this obvious difference, we have here chosen to improve the degree of coherence and to have a better control of its value and stability. This is partly at the expense of intensity, but a smaller intensity can be compensated by greater coherence in a speckle experiment. Low intensity and high coherence are also more compatible with the use of a CCD area detector, at least with the droplet algorithm. Currently, CCDs are read at a low rate (less than 1 MHz conversion frequency for Princeton Instruments), and our algorithm works if individual photons are easily identified (in practice, the intensity must be less than one-tenth of an X-ray per pixel in the main part of the detector).

Windows introduce strong degradation of the synchrotron radiation source properties. Here, the brilliance is decreased because the windows act as secondary sources in the beam trajectory.

## 5. Conclusions

In this paper, we have shown that excellent results can be obtained in static coherent experiments with the D2AM beamline. The discussion clearly shows that the optical performance is at a high level. Moreover, the set-up is stable for several hours and for  $q$  smaller than  $0.01 \text{ \AA}^{-1}$ . Removal of the Kapton windows will increase the degree of coherence and make its measurement more precise. The arrangement provides a tool for the study of slow processes, of small spatial extension (from 100 to 2000  $\text{\AA}$ ).

For the future of such measurements, focusing and monochromated beamlines from window-free undulators will be very efficient.

The authors wish to thank Mark Sutton for suggesting realistic calculations of the beam coherence, Erik Geissler, Jacques Mainville, René Caudron, Doug Abernathy and G. Grübel for fruitful collaboration, and René Caillot and Stephan Arnaud for technical help.

## References

- Abernathy, D. L., Grübel, G., Brauer, S., McNulty, I., Stephenson, G. B., Mochrie, S. G., Sandy, A. R., Mulders, N. & Sutton, M. (1998). *J. Synchrotron Rad.* **5**, 37–47.
- Bley, F., Livet, F., Leroux, J. C., Simon, J. P., Abernathy, D., Als-Nielsen, D., Grübel, G., Vignaud, G., Dolino, G., Legrand, J. F., Camel, D., Menguy, N. & Papoular, M. (1995). *Acta Cryst.* **A51**, 746–750.
- Brauer, S., Stephenson, G. B., Sutton, M., Brüning, R., Dufresne, E., Mochrie, S. G. J., Grübel, G., Als-Nielsen, J. & Abernathy, D. L. (1995). *Phys. Rev. Lett.* **74**, 2010–2013.
- Brown, W. (1993). Editor. *Dynamic Light Scattering*, p. 90. Oxford: Clarendon Press.
- Dierker, S. B., Pindak, R., Fleming, R. M., Robinson, I. K. & Berman, L. (1995). *Phys. Rev. Lett.* **75**, 449–452.
- Dufresne, E. (1995). PhD thesis, McGill University, Canada.
- Elleaume, P. (1986). Summer School on Synchrotron Radiation, Aussois. Grenoble: CNRS.
- Livet, F., Bley, F., Sutton, M., Mainville, J., Geissler, E., Dolino, G. & Caudron, R. (1998). To be published.
- McKechnie, T. S. (1975). *Opt. Commun.* **13**, 35–39.
- Mainville, J., Bley, F., Livet, F., Geissler, E., Legrand, J. F., Abernathy, D. L., Grübel, G., Mochrie, S. G. J. & Sutton, M. (1997). *J. Appl. Cryst.* **30**, 828–832.
- Mandel, L. & Wolf, E. (1995). *Optical Coherence and Quantum Optics*. Cambridge University Press.
- Mochrie, S. G. J., Mayes, A. M., Sandy, A. R., Sutton, M., Brauer, S., Stephenson, G. B., Abernathy, D. L. & Grubel, G. (1997). *Phys. Rev. Lett.* **78**, 1275–1278.
- Roth, M., Ferrer, J. L., Simon, J. P. & Berar, J. F. (1997). *ESRF Beamline Handbook*, p. 43. ESRF, Grenoble, France.
- Sutton, M., Mochrie, S. G. J., Greytak, T., Nagler, S. E., Berman, L. E., Held, G. A. & Stephenson, G. B. (1991). *Nature (London)*, **352**, 608–610.